Aerospace Science and Technology 84 (2019) 734–746

Contents lists available at ScienceDirect

Aerospace Science and Technology

www.elsevier.com/locate/aescte

Roles and mechanisms of casing treatment on different scales of flow instability in high pressure ratio centrifugal compressors

Xiao He, Xinqian Zheng *

Turbomachinery Laboratory, State Key Laboratory of Automotive Safety and Energy, Tsinghua University, Beijing, 100084, China

ARTICLE INFO

Article history:
Received 12 April 2018
Received in revised form 17 September 2018
Accepted 8 October 2018
Available online 15 October 2018

Keywords:
Centrifugal compressor
Casing treatment
Surge
Stall
Rotating instability

ABSTRACT

The development of single-stage high pressure ratio centrifugal compressors for small gas turbine engines is hindered by compressor flow instabilities with various temporal and spatial scales. In this paper, the effect of a self-recirculation casing treatment device for suppressing various scales of flow instability has been discussed. Rig tests of a high pressure ratio centrifugal compressor with and without a casing treatment device are performed, and transient pressure signals are measured at endwalls by fast response pressure transducers. By analyzing measured pressure signals in both time and frequency domain, the casing treatment device is found effective in eliminating rotating instability and stall at the impeller inlet at low speeds, as well as suppressing surge of the compression system at middle and high speeds. The flow recirculation process generated inside the casing treatment device removes the vortical structures at the impeller inlet tip section, therefore eliminating the regional rotating instability and stall. Besides, the casing treatment device turns the pressure rise characteristics of the impeller more negative by enhancing the impeller work input, but turns that of the vaned diffuser more positive by increasing the incidence at the vaned diffuser inlet. Combining both effects, mild surge and the deep surge are suppressed.

1. Introduction

Single-stage high pressure ratio centrifugal compressors are preferred in the aviation industry to reduce the manufacturing cost and the engine weight [1]. However, increasing the pressure ratio will lead to transonic inlet conditions that further deteriorates the complex flow field of compressors. As a result, the compressor stable flow range drops rapidly with increasing pressure ratios [2], which hinders the application of such compressor stages.

To date, mainly three groups of flow instabilities have been identified in compressors, namely surge, rotating stall, and rotating instability in descending order of their temporal and spatial scales [3]. Surge is the breakdown of the compression system that propagates through the streamwise direction. Its spatial scale is at the order of the streamwise length of the compression system, and its temporal scale is close to the system Helmholtz frequency. According to the oscillation intensity and the occurrence of reverse flows, the surge phenomenon can be further classified into mild surge and deep surge [4]. The nature of surge was unveiled by the lumped parameter model of Greitzer [5]. It is the characteristics of the compressor, the throttle, and the non-dimensional B parameter that govern the surge phenomenon. Rotating stall is the circumferential propagation of single or multiple low-momentum cells (or stall cells) that limits the compressor pressure rise. Its spatial scale is at the order of the compressor circumference, and its temporal scale is on the order of rotor or impeller passing frequency (RPF or IPF). Emmons et al. [6] proposed a definite phenomenological model about rotating stall: when the first stall cell is formed in a blade passage, it blocks the incoming flow and causes an incidence spike on the adjacent blade, which drives the adjacent blade to stall, and thus the stall cell rotates. Rotating instability is the pre-stall disturbance that is continually changing in amplitude and frequency. Its spatial scale is at the order of the compressor blade pitch, and its temporal scale is on the order of blade passing frequency (BPF) [7]. Rotating instability usually exists in cases with large tip gaps (i.e., over 3% of chord for axial compressors [3]), and its mechanism was proposed to be the circumferential movement of a radial vortex inside a blade passage [8].

Regarding centrifugal compressors, the pathology of flow instabilities across scales has been studied through both experiment and CFD approaches. The occurrence of rotating instability is commonly reported at the impeller inlet when operating at part speeds [9–12]. It could evolve into the inducer stall that appears as the symmetric blockage around all the annulus and limits the compressor pressure rise capability. The rotating stall is usually found at the inlet of the vaneless diffuser [9] or the vaned diffuser

* Corresponding author.
E-mail addresses: hex15@mails.tsinghua.edu.cn (X. He), zhengxq@tsinghua.edu.cn (X. Zheng).

https://doi.org/10.1016/j.ast.2018.10.015
1270-9638/

Nomenclature

A	area	m^2
B	blockage factor	
b	blade height	m
c	absolute velocity	m/s
c_p	specific heat capacity at constant pressure	J/(kg K)
c_s	slip velocity	m/s
m	mass flow rate	kg/s
r	distance in the radial direction	m
u	blade velocity	m/s
w	relative velocity	m/s
W	specific work	J/kg
Z	number of blades	
β	blade angle	deg
γ	heat capacity ratio	
π	stage total-to-total pressure ratio	
ρ	density	kg/m^3
σ	slip factor	
υ	kinematic viscosity	m^2/s

Abbreviations

BPF	blade passing frequency
IPF	impeller passing frequency
RSD	relative standard deviation
SP	stability parameter

Definition of non-dimensional parameters

Mu	impeller tip Mach number $\frac{u_2}{\sqrt{\gamma RT_{t1}}}$
Re	Reynolds number $\frac{u_2 b_2}{\upsilon_1}$
φ	flow coefficient $\frac{m}{4\rho_{t1}u_2 r_2^2}$
λ	work coefficient $\frac{c_p T_{t1}(\pi^{\frac{\gamma-1}{\gamma}}-1)}{\eta u_2^2}$
N_s	specific speed $\frac{2\varphi^{1/2}}{\lambda^{3/4}}$

Subscripts

1	impeller inlet (ambient)
2	impeller exit
4	diffuser exit
6	volute exit
f	front part
m	meridional component
r	recirculation flow/rear part
s	isentropic process
t	total quantity/tangential component
II	transducer location at impeller exit
IV	transducer location at diffuser exit

Superscripts

dat	case without a casing treatment device
rec	case with a casing treatment device

[13–15] when operating near the design speed. Such stall cells could be triggered either by spike signals within five rotor revolutions or by mode signals after tens of rotor revolutions. The surge patterns vary with speed. The mild surge usually precedes the deep surge at low speeds (small B parameter), but the deep surge will emerge abruptly at high speeds (large B parameter). The motivator of the surge also switches from the upstream impeller to the downstream diffuser when increasing the speed [9,12]. When the design pressure ratio is high, the centrifugal compressor will suffer from severe rotating instability and stall at impeller inlet at low speeds, as well as a narrow surge margin at high speeds [12]. Flow control methods that improve the compressor stability at the entire operating speeds are essential for such compressor stages.

Self-recirculation casing treatment is one of the passive flow control methods that have potentials to suppress flow instabilities across scales. It has been successfully applied to turbocharger centrifugal compressors for over 30 years [16], and it has also been tested in axial compressors recently [17]. A casing treatment device consists of front and rear slots and an annular cavity that links both slots together. The main effects of such devices are the flow recirculation and the swirl momentum injection. First, the low-momentum flow region at the impeller tip section is suctioned through the rear slot and re-injected through the front slot, thereby improving the impeller tip flow field as well as allowing the inducer to operate at a higher mass flow. Second, the recirculation flow has a pre-swirl by the rotating direction, which leads to a reduction in incidence and relative Mach number near the impeller tip. The flow recirculation and swirl injection processes have been confirmed in experiments [18] and LES simulations [19] at near surge conditions. The mass flow bleeding process at the rear slot is proposed to be dominant in setting the compressor performance [20].

Previous studies of the casing treatment device successfully extended the surge margin of turbocharger centrifugal compressors, where a vaneless diffuser is attached downstream, and the surge is often triggered at the impeller inlet. For high pressure ratio cases with vaned diffusers, however, the surge is often initiated by the vaned diffuser [12,13]. It is worth researching whether the further improved impeller stability by a casing treatment device could act against the instability of the vaned diffuser, thus extending the surge boundary. Regarding local flow instabilities with sub-circumference scales, roles of casing treatment devices are also yet to be determined.

The motivation of this paper is to detail the effects of self-recirculation casing treatment on different scales of flow instabilities in high pressure ratio centrifugal compressor stages. To achieve this, a high pressure ratio centrifugal compressor for lightweight helicopter engines is investigated through the experimental approach, where flow instabilities across scales were reported at various operating speeds of the compressor [12]. As a start, the experimental methodology and the investigated case is explained in detail. Then, performances of the stage and the components with and without a casing treatment device are analyzed and compared. Finally, the phenomenon and mechanisms of casing treatment devices on eliminating rotating instability and stall, as well as on suppressing mild surge and deep surge are discussed respectively.

2. Methodology

2.1. Test compressor

The investigated high pressure ratio centrifugal compressor is an in-house prototype design, whose specifications are presented in Table 1. The motivation of developing such a compressor is to replace the existing axial-centrifugal multistage compressor with the single-stage centrifugal one. To fit the test bench, the compressor has been scaled to about half of its designed size following the similitude criteria of turbomachinery. The impeller and the vaned diffuser were manufactured by flank milling of titanium alloy and stainless steel, respectively. The vaned diffuser disc was installed

Table 1
Specification of datum compressor TTL-1-scale.

Parameters	Symbols	Values
Number of impeller blades	Z_I	24
Leading edge hub radius	r_{1h}/r_2	0.26
Leading edge tip radius	r_{1t}/r_2	0.65
Number of diffuser vanes	Z_D	19
Diffuser leading edge radius	r_3/r_2	1.10
Diffuser trailing edge radius	r_4/r_2	1.48
Impeller tip Mach number	Mu	1.80
Stage total pressure ratio	π_{1t-6t}	6.18
Reynolds number	Re	1.34×10^5
Flow coefficient	φ	0.06
Work coefficient	λ	0.75
Specific speed	N_s	0.61

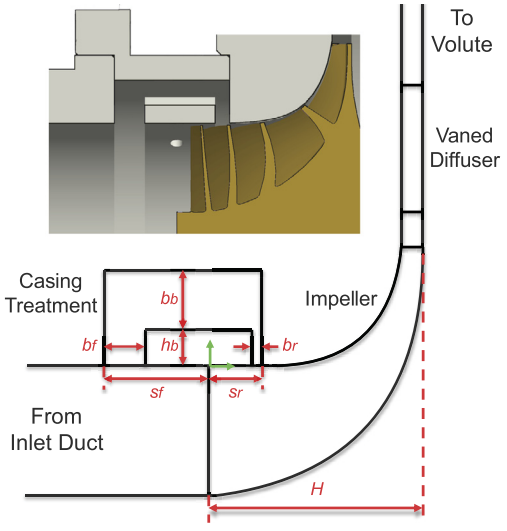

Fig. 1. Schematic of the self-recirculation casing treatment.

in the casing. To collect the pressurized air, a volute was attached downstream of the vaned diffuser.

2.2. Casing treatment device

Schematic of a self-recirculation casing treatment is illustrated in Fig. 1. The casing treatment device is parameterized by six independent parameters, namely rear slot distance (s_r), rear slot width (b_r), front slot distance (s_f), front slot width (b_f), channel height (h_b) and channel width (b_b). Those parameters are often normalized by the axial length of the impeller (H).

The effect of casing treatment device on enhancing the stable flow range can be roughly described by a simplified 1D flow model. Assuming surge is initiated at the impeller, the compressor surge mass flow with and without the casing treatment can be calculated as follows:

$$m_s^{rec} = m_{\min}^{rec} - m_r \tag{1}$$

$$m_s^{dat} = m_{\min}^{dat} \tag{2}$$

where $m_{\min}$ is the minimum mass flow allowed by the impeller, and m_r is the recirculation mass flow. Assuming that the $m_{\min}$ for both cases are almost the same, the above equations can be combined, yielding:

$$\frac{m_s^{dat} - m_s^{rec}}{m_s^{rec}} \approx \frac{m_r}{m_s^{rec}} \tag{3}$$

where the left-hand term represents the extension of the surge boundary, and the right-hand term represents the recirculation ratio at the surge condition. Such a linear trend is examined in Fig. 2, where the presented data are obtained from a literature survey and a parametric study. It is illustrated that most cases fall in the linear band, indicating the recirculation ratio is essential in determining the effectiveness of casing treatment devices. Cases violate the linear trend either have counter-swirl vanes installed in slots, or have a strong reverse flow pattern at the impeller inlet, both of which are out of the scope of the current paper.

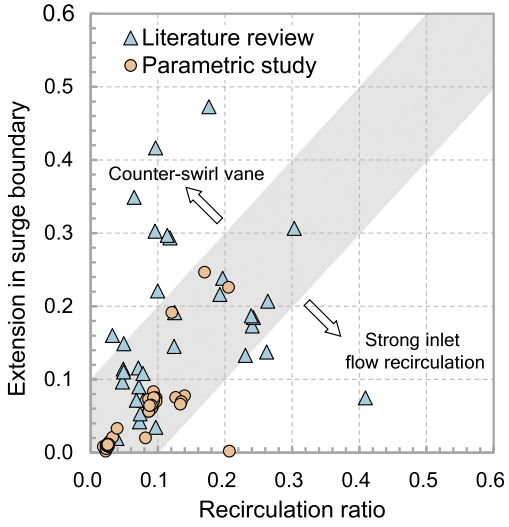

Fig. 2. Trend of the surge boundary extension versus recirculation ratio, steady RANS data [20–30].

Table 2
Parameter values of the casing treatment device.

Parameters	Min	Design	Max
Rear slot distance (s_r/H)	15.6%	24.9%	34.3%
Rear slot width (b_r/H)	2.3%	9.3%	9.3%
Front slot distance (s_f/H)	29.2%	48.7%	68.1%
Front slot width (b_f/H)	4.9%	19.5%	19.5%
Channel height (h_b/H)	3.9%	11.5%	15.6%
Channel width (b_b/H)	6.3%	16.1%	25.3%

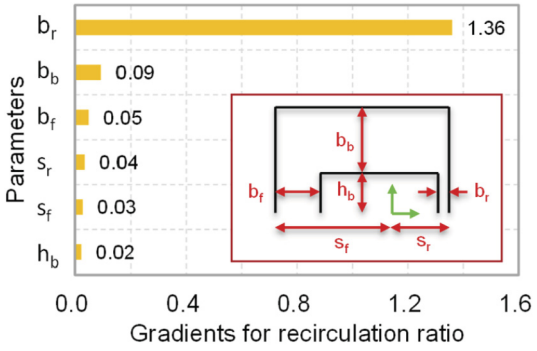

Fig. 3. The sensitivity of parameters on recirculation ratio.

During the design phase of the casing treatment device, a parametric study was carried out through single-passage steady RANS simulations [21]. The design space is given in Table 2. In total, 26 casing treatment devices were investigated on 80%, 90% and 100% speed lines of the compressor, and a quadratic response surface model was constructed to approximate the parametric database. To evaluate the sensitivity of each parameter, the partial derivative of the recirculation ratio with respect to each parameter is compared based on the response surface model. It is illustrated in Fig. 3 that the rear slot width is the definitive parameter on the recirculation ratio, while other parameters are relatively less critical.

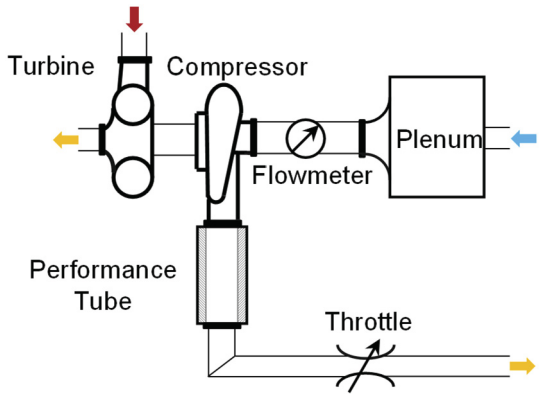

Fig. 4. Schematic of the test rig.

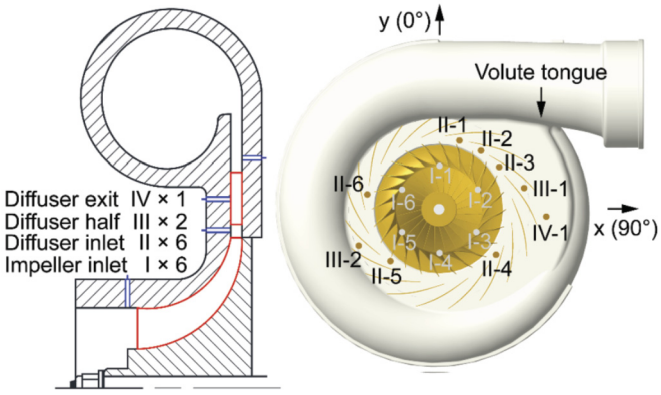

Fig. 5. Schematic of transducers setup.

The final design of the rear slot width considers both the desired extension in the surge boundary and the affordable penalty in efficiency. Other parameters are designed to make the device as compact as possible without much loss in the recirculation ratio. The non-dimensionalized parameter values of the final design are given in Table 2. During the manufacturing phase, the casing treatment device is flank milled in separate parts to improve the smoothness of surfaces. The mechanical support between the lower channel wall and the upper channel wall is achieved by six symmetrically distributed struts. Transducers can be installed in screw holes of each strut.

2.3. Experimental method

Performances of compressors are measured on a turbocharger compressor test rig, as illustrated in Fig. 4. A magnetoresistive sensor at the impeller inlet measures the rotation speed. A Venturi flowmeter in the inlet duct measures the mass flow rate. To obtain the pressure ratio and the isentropic efficiency of the compressor stage, total pressures and total temperatures are measured at the upstream plenum and the downstream tube by pressure sensors and thermometers. The occurrence of surge can be diagnosed by the relative standard deviation (RSD) of the measured unsteady pressure at the upstream plenum. In addition to the conventional rig test procedure, unsteady pressures on compressor passage walls are measured by fifteen fast response pressure transducers whose labels and locations are illustrated in Fig. 5. Measurement errors of each equipment are summarized in Table 3. The experiment was carried out from large to small mass flows and from low to high speeds. Data of each operating point are recorded only when the variation of the isentropic efficiency and the corrected rotation speed is within ±0.1% and ±200 RPM in one minute. Repetitive tests demonstrate that the variation of the measured pressure ratio at an identical mass flow rate is within 0.1, and the variation of the measured mass flow at the deep surge onset is within 3×10^{-3} kg/s. More detailed experimental settings can be found in our previous work [12].

Table 3
Measurement error of the test facility.

Equipment name	Error
Flowmeter	$\pm 2.36 \times 10^{-3}$ m^3/s (near choke)
Pressure sensor	±0.05% full-scale range
Thermometer	±0.6 K
Pressure transducer	±0.10% full-scale range

Table 4
Diagnosis criteria for flow instabilities.

Phenomena	Diagnosis criteria
Deep surge	(1) Inlet pressure RSD over 10% (2) Reverse flow occurs (3) Periodic signal around 1 Hz (4) Amplitude over dynamic pressure
Mild surge	(1) Inlet pressure RSD within 1–10% (2) No reverse flow occurs (3) Sinusoidal signal around 10 Hz (4) Amplitude within dynamic pressure
Stall	(1) Inlet pressure RSD below 1% (2) Hump in spectrum from 10–90% IPF (3) Reach the peak pressure ratio
Rotating instability	(1) Inlet pressure RSD below 1% (2) Hump in spectrum from IPF to BPF

3. Compressor performance

3.1. Stage performance

To diagnose the instability phenomena inside compressors, several diagnosis criteria are adopted. Firstly, the RSD value of the inlet plenum pressure is checked. Noticing the surge phenomenon propagates in the streamwise direction, a high value of the inlet pressure RSD corresponds to the occurrence of the surge. Empirical threshold values of 1% and 10% are capable of differentiating non-surge, mild surge and deep surge in the current case, but those threshold values may vary with different test rigs and test compressors. Secondly, unsteady pressure traces on compressor passage walls are analyzed. The deep surge signal is featured by low-frequency, periodic, and violate fluctuations, where the period is around 1 Hz, and the amplitude is over one dynamic pressure (i.e., $\rho_1 u_{1t}^2/2$ or $\rho_1 u_2^2/2$). Flow reversal in the deep surge cycle can be detected by the drastic increase of the impeller inlet pressure, which is caused by the discharging of the downstream plenum. The mild surge signal is featured by low-frequency, sinusoidal, and moderate fluctuations, where the period is around 10 Hz and the amplitude is within one dynamic pressure. No sign of flow reversal exists. Finally, frequency spectrums of measured unsteady pressures are examined. A notable hump between 10–90% of IPF in the spectrum corresponds to the scale of the stall signal, which also coincides with the peak pressure ratio condition of the nearby component. A notable hump between IPF and BPF corresponds to the scale of the rotating instability signal. The diagnosis criteria for flow instabilities are summarized in Table 4.

Performance and stability maps of the investigated compressor with and without the casing treatment device are shown in Fig. 6. Within the measured speed lines, operating conditions including deep surge, mild surge, stall, rotating instability, and stable state are identified. According to Fig. 6, the role of the casing treatment device on suppressing compressor flow instabilities is

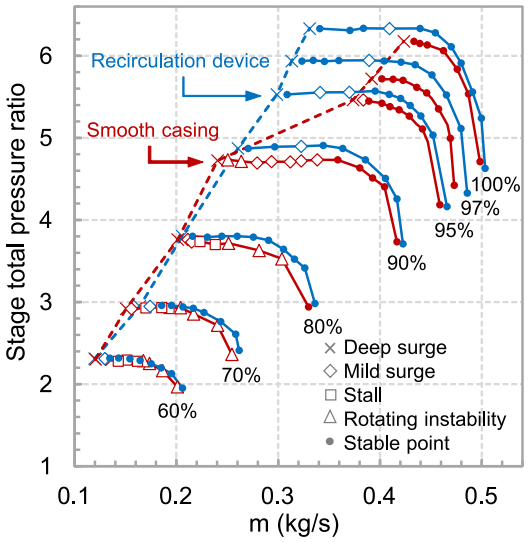

Fig. 6. Performance and stability map comparison. (For interpretation of the colors in the figure(s), the reader is referred to the web version of this article.)

twofold. For rotating instability and stall occurring at the impeller inlet at 60–90% design speed, they are successfully eliminated by the casing treatment device. For mild surge and deep surge, their strength has been evidently suppressed by the casing treatment device. At 90% design speed, the casing treatment device successfully squeezes the mild surge zone from a visible band to a single point. At 95–100% design speed, deep surge of the smooth casing case has been suppressed to mild surge, and thus the deep surge boundary is further extended.

3.2. Component performance

A clear criterion to diagnose the stability of the compression system is to check the sign of the total-to-static pressure ratio slope. The compression system remains stable when the slope is no greater than zero:

$$\frac{\partial(p_4/p_{1t})}{\partial m} \le 0 \tag{4}$$

The stage total-to-static pressure ratio of the current case can be divided into the impeller part and the vaned diffuser part. Thus, the criterion becomes:

$$\frac{1}{\pi_{1t-IV}}\frac{\partial \pi_{1t-IV}}{\partial m} = \underbrace{\frac{1}{\pi_{1t-II}}\frac{\partial \pi_{1t-II}}{\partial m}}_{\text{Impeller}} + \underbrace{\frac{1}{\pi_{II-IV}}\frac{\partial \pi_{II-IV}}{\partial m}}_{\text{Vaned diffuser}} \le 0 \tag{5}$$

A qualitative way to judge the stability of a component is to check the sign of its pressure curve slope. The impeller and the vaned diffuser pressure characteristics are shown in Fig. 7. The impeller pressure ratio is calculated using the circumferential-averaged (i.e., II-2, II-4, II-5, and II-6) mean pressure at the impeller exit, and the vaned diffuser pressure ratio is calculated using the mean static pressure from the diffuser passage near the volute tongue (i.e., II-3 and IV-1). In Fig. 7(a), the casing treatment device increases the peak pressure ratio of the impeller by 2–4% relatively and turns the slope of the impeller pressure characteristics more negative near low mass flow conditions. The stability of the impeller is therefore improved by the casing treatment device, especially at middle and high speeds. On the other hand, it is interesting to find in Fig. 7(b) that the casing treatment device deteriorates the vaned diffuser stability, as its pressure characteristics turn more positive near low mass flow conditions.

A quantitative way to compare their stability is to calculate the value of each right-hand side term in Eq. (5), which is named as the stability parameter. To compute the slope of pressure characteristics, the pressure characteristics of selected operating points are fitted by natural cubic splines. Thus, their slopes can be directly computed from spline formulas. The stability parameters of the impeller are plotted against that of the vaned diffuser in Fig. 8. The figure can be divided into four quadrants: the diffuser is unstable in the first and the second quadrant, the impeller is unstable in the first and the fourth quadrant, while both components are stable in the third quadrant. It is generally found that the casing treatment device has pushed dots from the right-bottom corner to the left-up corner, indicating an improvement in the impeller stability but a decline in the diffuser stability.

Combining the effect on the impeller and the vaned diffuser pressure characteristics together, the stage pressure characteristics presented in Fig. 6 can be better comprehended. At low speeds, the casing treatment device slightly improves the impeller stability but deteriorates the vaned diffuser stability, which in total produces a neutral influence on the stage pressure rise and thus fails to suppress surge behaviors. At middle and high speeds, although the vaned diffuser stability turns worse, the impeller stability has been greatly improved. Therefore, the stage pressure characteristics have been stabilized, and the mild surge and the deep surge have been suppressed.

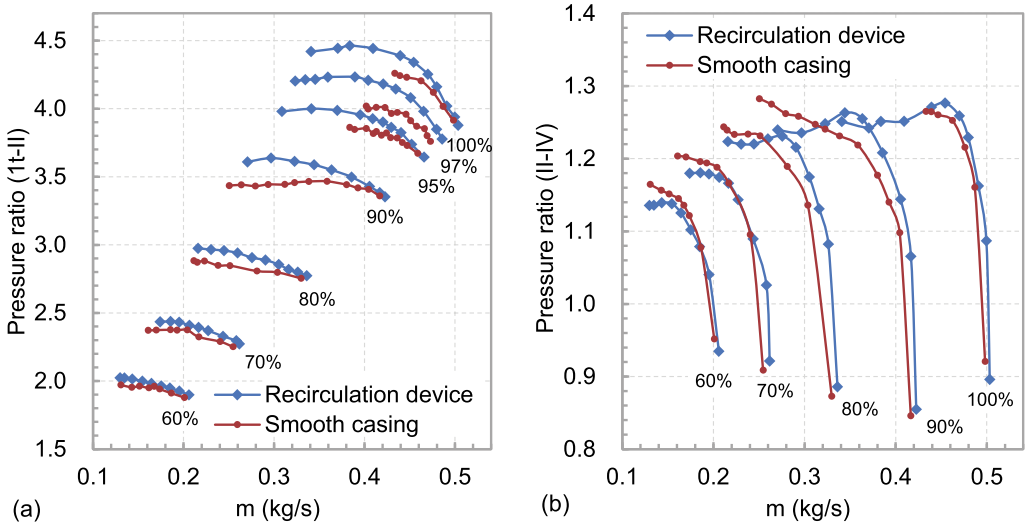

Fig. 7. Component performance comparison: (a) impeller and (b) vaned diffuser.

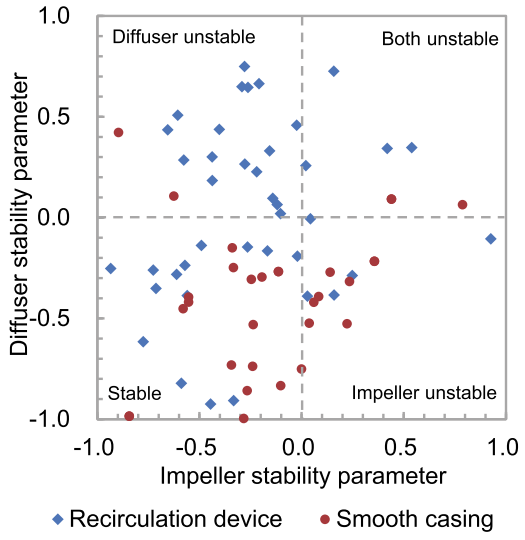

Fig. 8. Stability parameter comparison.

4. Elimination of rotating instability and stall

4.1. Observation in experiment at low-speeds

To compare the instability composition with and without the casing treatment device, fast Fourier analysis was performed based on the measured transient pressure data at the impeller inlet. Frequency spectrums across the 60% design speed lines are presented as a representative case in Fig. 9, where the frequency is normalized by the IPF and the Fourier coefficient is normalized by the time-averaged total-to-static pressure ratio measured by the transducer. In each frequency spectrum figures, two peaks representing the IPF and the BPF are quickly identified since their expected frequency values can be calculated by the shaft speed and the impeller blade number. Signals of IPF, BPF and their harmonics are not necessarily induced by flow instabilities. Instead, they are natural references to help distinguish the scale of flow instabilities.

For the smooth casing case in Fig. 9(a), a broadband hump between IPF and BPF is observed from 0.20 kg/s to 0.16 kg/s, indicating the occurrence of rotating instability. When further reducing the mass flow rate to 0.14 kg/s, the impeller reaches its peak pressure ratio condition (Fig. 7(a)), and a second hump emerges and develops below the IPF, indicating the occurrence of the stall. Finally, the compression system enters into mild surge and deep surge.

The hump structure in frequency spectrums indicates the continuous change of the pressure signal in its period and amplitude, which is related to vortical structures. The evolution of rotating instability and stall humps is detailed in Fig. 10. The averaged hump central frequencies of transducer I-1 to I-6 are plotted against the mass flow, and the standard deviations along the circumference are represented by error bars. It is illustrated that the rotating instability grows in scales when decreasing the mass flow, where the central frequency reduces from 28% to 6% BPF. When the rotating instability evolves into the stall, the central frequency of both humps stays constant at around 6% BPF and 16% IPF, respectively.

For the case with the casing treatment device in Fig. 9(b), no apparent source of pressure signals exist except for the IPF, the BPF, and their harmonics before the surge onset. The casing treatment device is therefore effective in eliminating rotating instability and stall at the impeller inlet, where the casing treatment device is installed.

Time-averaged impeller inlet total-to-static pressure ratios are compared in Fig. 11, where dots represent the circumferential-averaged value and error bars indicate the standard deviation. Along with experimental results, the theoretical isentropic solution of the smooth casing case is plotted for reference, as computed in the following:

$$\frac{p_{I,s}}{p_{1t}} = \left(1 + \frac{\gamma - 1}{2} Ma_1\right)^{-\frac{\gamma}{\gamma - 1}} \tag{6}$$

where the Mach number is calculated using the inlet volumetric flow rate, the inlet duct diameter, and the total temperature in the inlet plenum.

The isentropic solution ignores the piping loss between the inlet plenum and the inlet duct, whose amplitude is empirically proportional to the square of the mass flow rate. From Fig. 11, it is confirmed at high mass flow conditions of the smooth casing case that the measured pressure ratio is smaller than the theoretical one. The higher the mass flow, the more evident the deviation becomes. The isentropic solution also supposes a uniform velocity

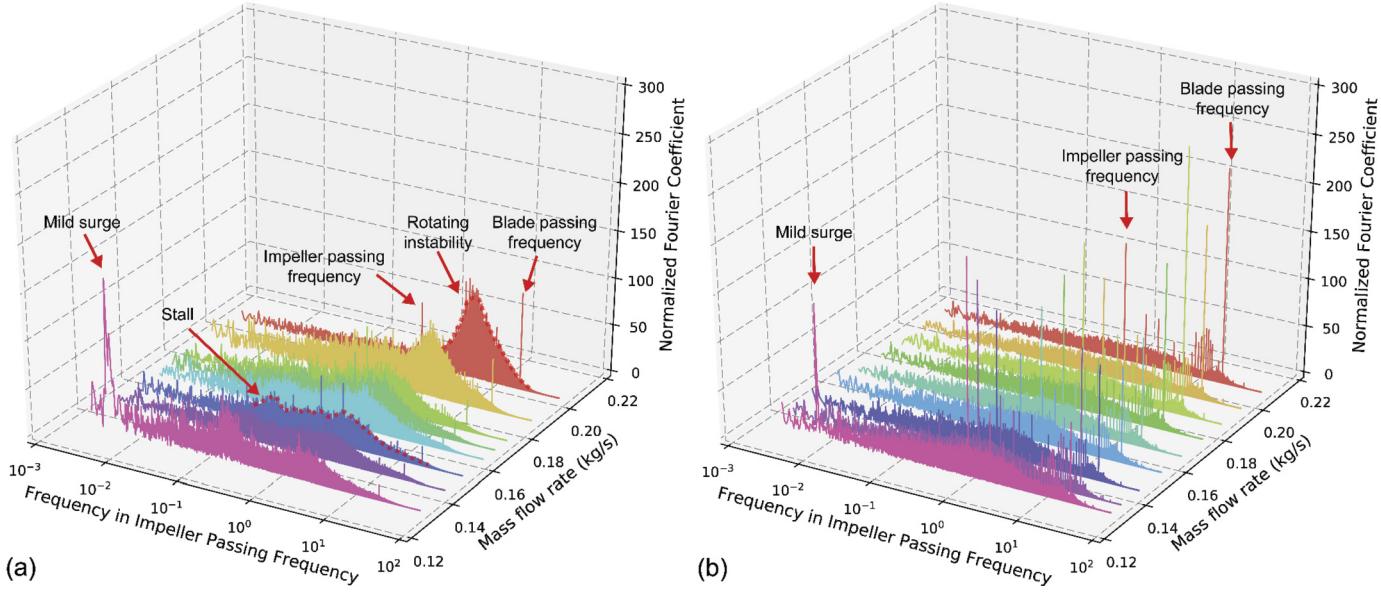

Fig. 9. Impeller inlet (I-1) frequency spectrum at 60% speed: (a) smooth casing and (b) casing treatment.

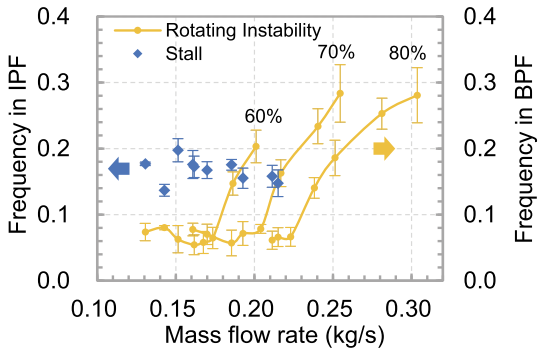

Fig. 10. Variation of the central frequency of rotating instability and stall humps of the smooth casing case, mean value from I-1 to I-6.

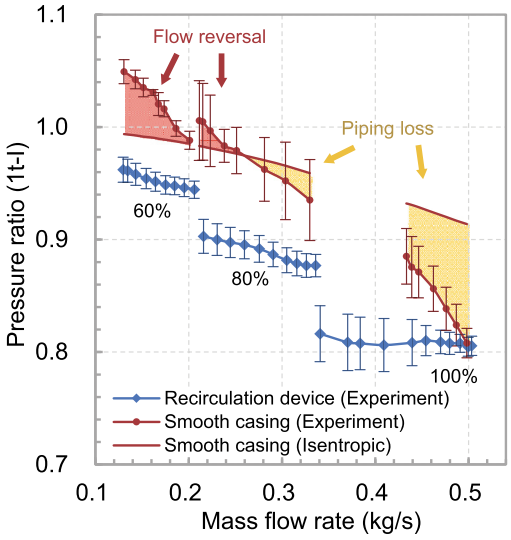

Fig. 11. Comparison of impeller inlet pressure, mean value from I-1 to I-6.

profile pointing to the downstream. If there is no reverse flow, the highest possible value of the total-to-static pressure ratio should be the isentropic solution. From Fig. 11, however, it is found at low mass flow conditions of the smooth casing case that the measured pressure ratio surpasses the isentropic one. Such results indicate the flow reversal at the impeller inlet casing section, where the high-energy flow in impeller passages reverses back and increases the local pressure. The lower the mass flow, the more severe the flow reversal becomes. Combined with Fig. 6, the flow reversal is generally found to coincide with the appearance of rotating instability and stall. The high pressure at the casing will consequently generate a radially-inward pressure gradient, which will lead to a streamline curvature in the meridional plane.

The measured pressure ratio curve of the casing treatment case is expected to intersect with that of the smooth casing case when there is no mass flow passing through the casing treatment device. The casing treatment device is in the recirculating mode when the operating mass flow is lower than that of the intersection point. Otherwise, it is in the bypassing mode. From Fig. 11, the only intersecting point exists at the choke condition of the design speed. The casing treatment device is thus on recirculation mode under most operating conditions, which is caused by the matching between the impeller and the vaned diffuser. Besides, the pressure ratio curves of the casing treatment case are evidently lower than that of the smooth casing case. This will generate a radially-outward pressure gradient and thus a curvature in the meridional streamline.

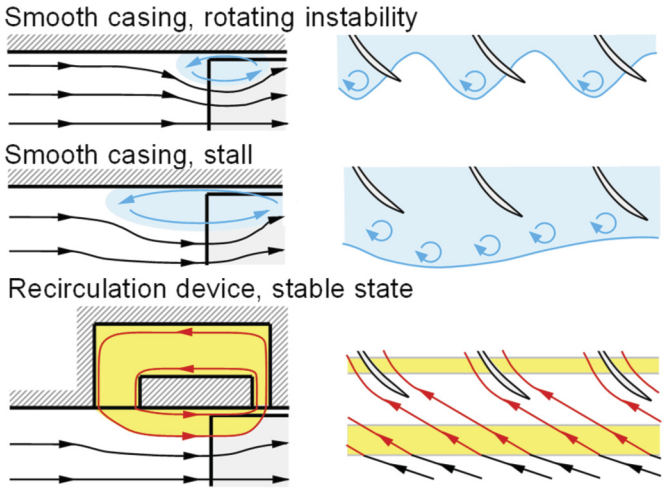

Fig. 12. Conceptual sketch of impeller inlet flow structures.

4.2. Flow mechanism on local flow structure

Based on the observation from experiments, the detected rotating instability and stall in this case are featured as backward traveling vortical flows, whose spatial scales are at the order of the impeller inlet blade pitch and the impeller inlet circumference, respectively. A radially-inward pressure gradient exists at the impeller inlet tip section, which leads to curvilinear streamlines in the meridional plane. On the other hand, neither reverse flows nor vortices exist at the impeller inlet tip section of the casing treatment case. The radially-outward pressure gradient at the impeller inlet tip section also results in curvatures of meridional streamlines.

The conceptual sketch of impeller inlet flow structures is illustrated in Fig. 12. For rotating instability, its mechanism in axial compressors has been determined as the unsteady circumferential movement of a radial vortex [8]. The inducer of centrifugal compressors is much similar to a rotor of axial compressors. Therefore, similar mechanisms are expected. Previous research numerically obtained the radial vortex structure in a centrifugal compressor [14], but the causal link between the vortex and the rotating instability phenomena is not clear. The current research possibly captured the near-casing end of the radial vortex, which generates the hump in frequency spectrums. When the compressor is further throttled, the vortical flow of rotating instability is proposed to develop in size from the sub-passage scale to the multi-passage scale, which leads to the inducer stall. Such developments were confirmed in previous axial [31] and radial [32] cases via pressure and velocity measurements. When the casing treatment device is applied, the blockage at the impeller inlet tip section will be eliminated by the recirculation process, thus the elimination of rotating instability and stall. The relieve of the inlet blockage was also presented through velocity measurements [32,33]. To complement the pressure and flow analysis in current research, more evidence from unsteady simulations are needed in the future.

5. Suppression of mild surge and deep surge

5.1. Observation in experiment at middle-speeds and high-speeds

Frequency spectrums of the vaned diffuser inlet pressure at 90% speed are compared in Fig. 13. For the smooth casing case in Fig. 13(a), a discrete peak near the system Helmholtz frequency (around 10 Hz in this case) exists in a band of mass flows, ranging from 0.34 kg/s to 0.28 kg/s. For the case with the casing treatment

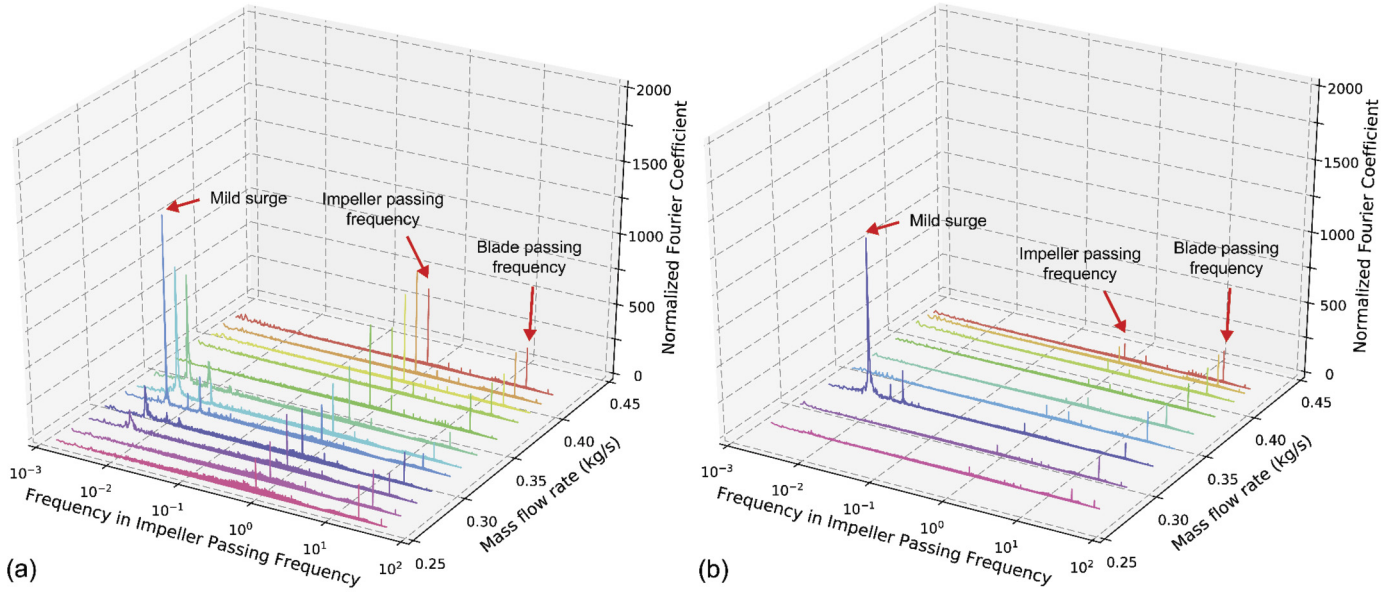

Fig. 13. Diffuser inlet (II-3) frequency spectrum at 90% speed: (a) smooth casing and (b) casing treatment.

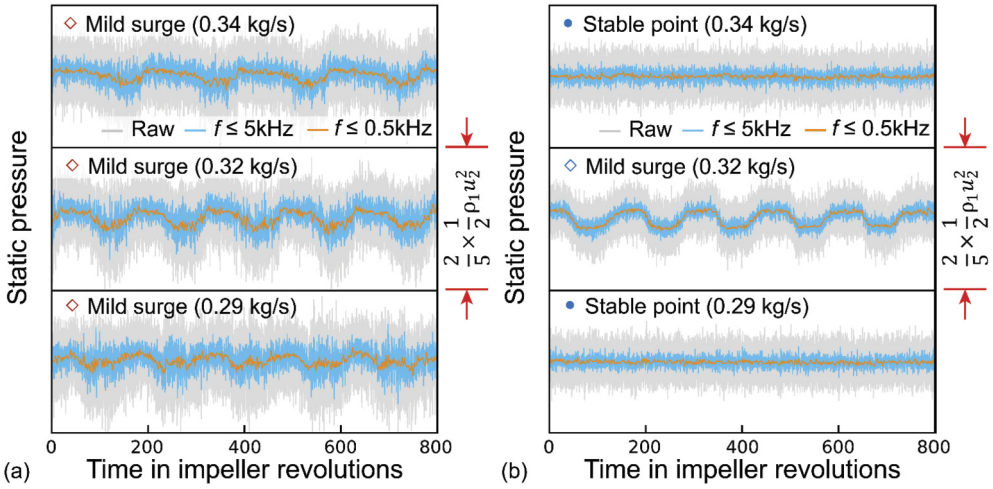

Fig. 14. Static pressure traces at the vaned diffuser inlet (II-3) of 90% design speed: (a) smooth casing and (b) casing treatment.

device in Fig. 13(b), the mild surge zone has been successfully squeezed from a wide region to a point at 0.32 kg/s.

To complement the discussion via frequency spectrums, static pressure traces at the vaned diffuser inlet near mild surge conditions are compared in Fig. 14. The raw data is low-pass filtered by the cutoff frequency of 5 kHz and 0.5 kHz, which is about 2.8 times and 28% of IPF, respectively. Subplots in each figure row share the same vertical axis scale. For the smooth casing case illustrated in Fig. 14(a), sinusoidal mild surge pressure waves are evident at all given mass flow conditions. For the casing treatment case presented in Fig. 14(b), the mild surge wave only exist at 0.32 kg/s, which has a similar level of amplitude and period to that of the smooth casing case. No evident large-scale wave structures can be observed at 0.29 kg/s and 0.34 kg/s. Hence, the casing treatment successfully suppressed the mild surge at those mass flows.

Frequency spectrums of the vaned diffuser inlet pressure at the 95% design speed are compared in Fig. 15. From Fig. 15(a), the smooth casing case directly enters into the mild surge condition at 0.38 kg/s without preceding rotating instability and stall occurring in either component. The compressor then operates into the deep surge condition when throttling to 0.37 kg/s. Because of the violent oscillation of the mass flow, the deep surge condition is not plotted in the three-dimensional frequency spectrum. From Fig. 15(b), the casing treatment device successfully suppresses the deep surge condition to a mild surge state, which delays the deep surge onset from about 0.37 kg/s to 0.30 kg/s. A long-lasting, stable state exists between mild surge and deep surge states, which is similar to the scenario at 90% speed.

The casing treatment device can effectively suppress deep surge at higher speeds in a similar manner. Static pressure traces at the vaned diffuser inlet at the 100% speed are compared in Fig. 16. At 0.44 kg/s, both cases with and without the casing treatment are free of low-frequency disturbance. When throttling to around 0.42 kg/s, the smooth casing case presents deep surge wave patterns with a pressure breakdown phase followed by a pressure recovery phase. For the casing treatment case, however, the deep surge pattern has been suppressed to the mild surge at a similar mass flow condition. When further throttling the compressor, the mild surge vanishes and the compressor stably operates at 0.37 kg/s. Finally, the compression system enters deep surge at around 0.33 kg/s.

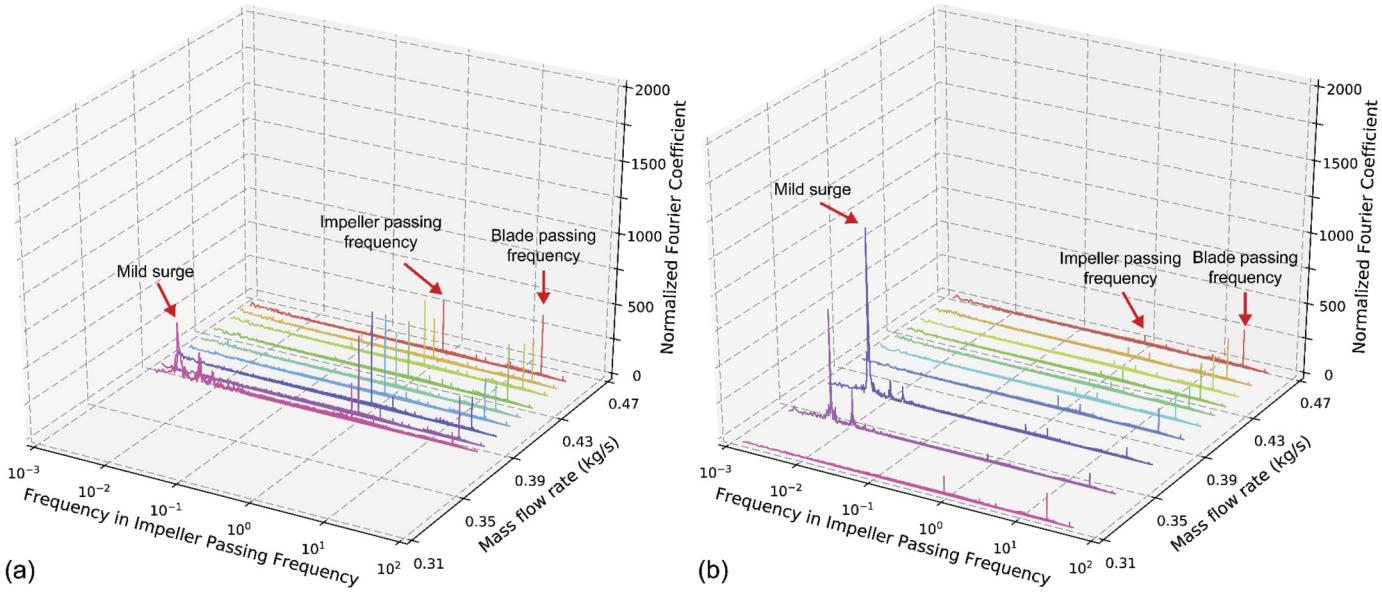

Fig. 15. Diffuser inlet (II-3) frequency spectrum at 95% speed: (a) smooth casing and (b) casing treatment.

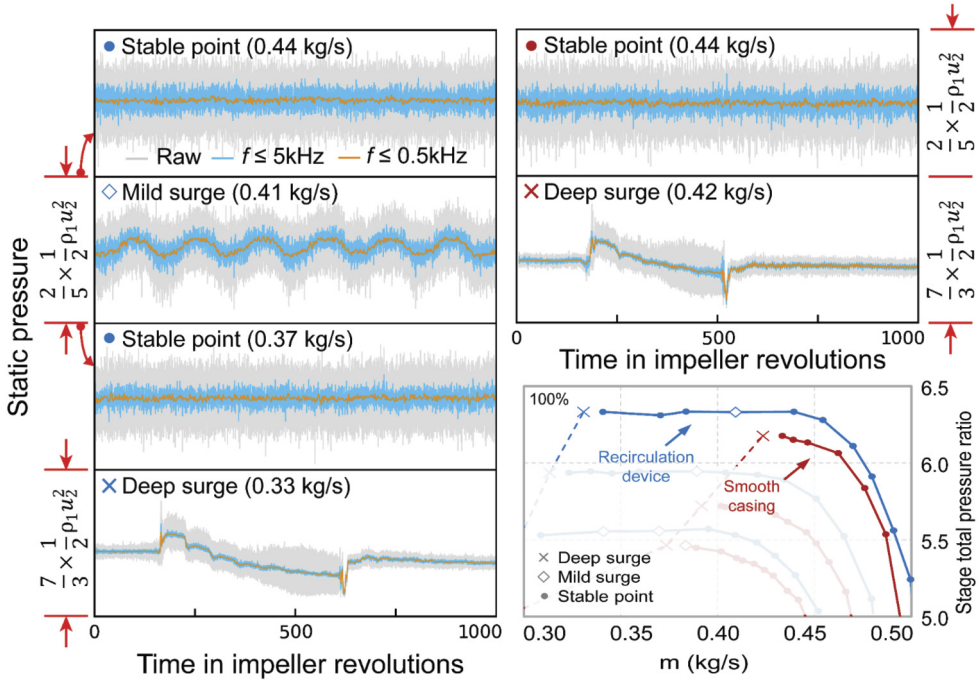

Fig. 16. Static pressure traces at vaned diffuser inlet (II-3) of 100% design speed.

5.2. Flow mechanism on impeller pressure characteristics

It is illustrated in Fig. 7(a) that the casing treatment enhances the impeller stability by turning its pressure rise slopes more negative. The impeller pressure rise characteristics can be increased through improving the work input or the efficiency. Neglecting the heat transfer on the solid walls of the vaned diffuser and the volute, the impeller work input can be fairly presented by the stage total temperature ratio given in Fig. 17(a). It is illustrated that slopes of work input characteristics at all speeds have been turned more negative near low mass flow conditions, which contributes to more negative slopes of pressure characteristics in Fig. 7(a). The impeller efficiency is included in the stage efficiency denoted in Fig. 17(b). When approaching low mass flow conditions, the efficiency of the casing treatment case is found to drop at a slightly steeper slope, which counteracts with the decreased slopes of pressure characteristics in Fig. 7(a). Therefore, the casing treatment device stabilizes the impeller by enhancing the impeller work input, but the induced efficiency loss at low mass flows destabilizes the impeller.

To help understand the mechanism for improving the impeller work input, a simple one-dimensional model was adopted. According to the rear slot location of the casing treatment device, the impeller can be divided into a front part and a rear part. The specific work input of the impeller with and without a casing treatment device can be written as follows:

$$\Delta W^{rec} = \left(1 + \frac{m_r}{m}\right)\Delta W_f^{rec} + \Delta W_r^{rec} \tag{7}$$

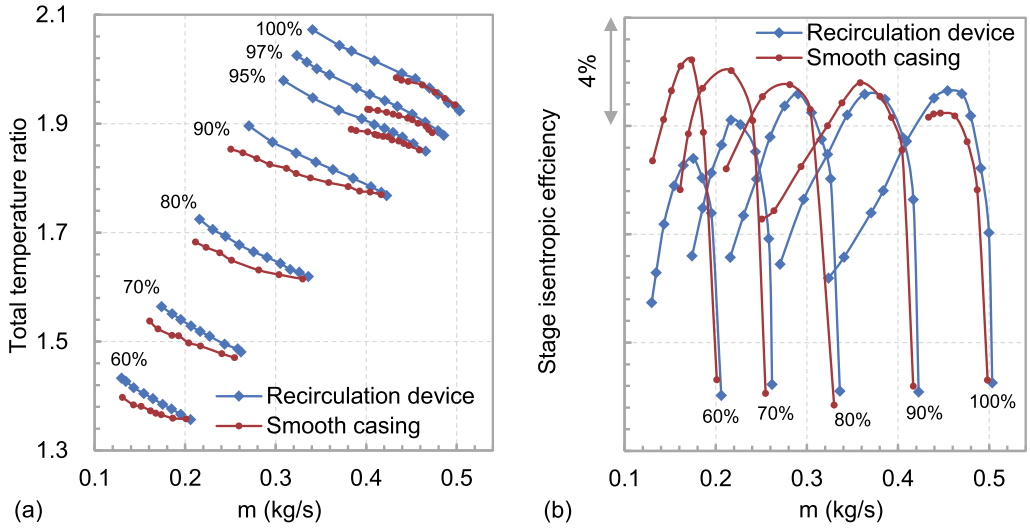

Fig. 17. Comparison of (a) stage total temperature ratio and (b) stage isentropic efficiency.

$$\Delta W^{dat} = \Delta W_f^{dat} + \Delta W_r^{dat} \tag{8}$$

Assuming the change of the specific work input of both impeller parts are limited, the impeller work input increment can be approximated as the product of the work input ratio and the recirculation ratio:

$$\frac{\Delta W^{rec} - \Delta W^{dat}}{\Delta W^{dat}} \approx \frac{\Delta W_f^{dat}}{\Delta W^{dat}} \frac{m_r}{m} \tag{9}$$

The work input ratio can be calculated by compressor mean-line analysis when the impeller geometry and the operating condition are known, as well as the deviation and the efficiencies are assumed (i.e., 0 deg and 100% as the simplest case). The recirculation ratio could not be calculated from the available data. Instead, it has been obtained through preliminary steady RANS simulations where the volute and the single passage of the impeller, the casing treatment device and the vaned diffuser were meshed, and the turbulence closure was achieved by the SST-CC model. Similar to a previous study [22], a linear correlation is applied between the recirculation ratio and the mass flow:

$$\frac{m_r}{m} = km + b \tag{10}$$

Characteristics of the work input ratio and the recirculation ratio are illustrated in Fig. 18. Finally, the predicted and the measured work input increments are compared in Fig. 19. The simple 1D model qualitatively agrees with the experiment, which implies the importance of the work input ratio and the recirculation ratio on improving the impeller work input. The former one is determined by the loading distribution of the impeller and the rear slot position of the casing treatment device. The later one is decided by the rear slot width.

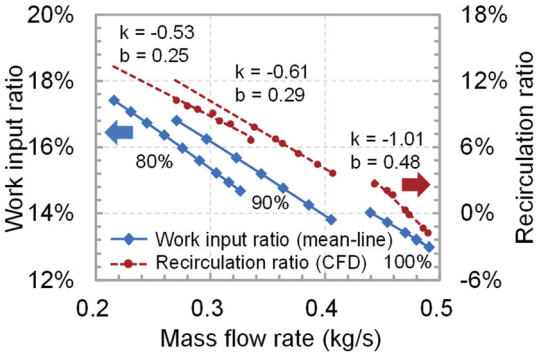

Fig. 18. Characteristics of the work input ratio and the recirculation ratio.

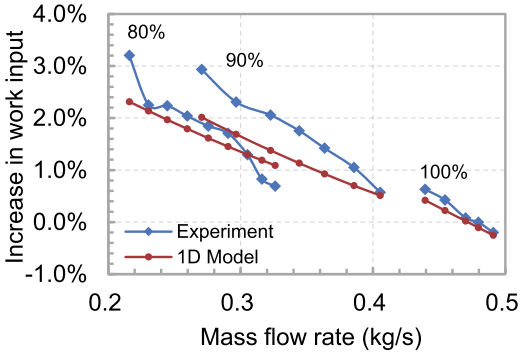

Fig. 19. Comparison of work input increment between experiment and 1D model.

5.3. Flow mechanism on vaned diffuser pressure characteristics

It is illustrated in Fig. 7(b) that the casing treatment device deteriorates the vaned diffuser stability as the diffuser reaches its peak pressure rise at a much larger mass flow. The performance of vaned diffusers is dominated by the diffuser inlet incidence [34], and an increased incidence at a given mass flow will lead the diffuser instability to occur in advance.

According to the impeller exit velocity triangle in Fig. 20, there are two ways to increase the impeller exit flow angle α_2. The first approach is to reduce the slip velocity c_s. Given the same meridional velocity component c_{m2}, a decreased slip velocity leads to an increased tangential velocity component c_{u2}, and thus the flow angle increases. The slip velocity is often non-dimensionalized as the slip factor σ:

$$\sigma = 1 - \frac{c_s}{u_2} \tag{11}$$

The second approach is to reduce the meridional velocity component. Given the same slip velocity, a decreased meridional velocity component leads to an increased tangential velocity component, both of which will increase the flow angle. The meridional velocity can be non-dimensionalized as the impeller exit flow coefficient:

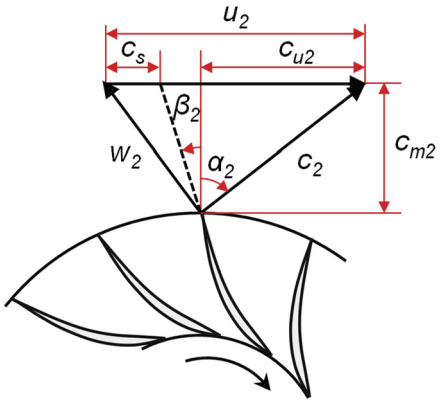

Fig. 20. Impeller exit velocity triangle.

$$\varphi_2 = \frac{c_{m2}}{u_2} \tag{12}$$

It should be noted that both approaches will lead to an increased tangential velocity component, which is in accordance with the enhanced impeller work input as observed previously.

To quantify the effect of the slip factor and the impeller exit flow coefficient on the flow angle, the compressor mean-line analysis was performed based on the test data. The impeller exit velocity triangle is calculated as follows:

$$c_{u2} = \frac{c_p(T_{t2} - T_{t1})}{u_2} \tag{13}$$

$$c_{m2} = \frac{\sigma u_2 - c_{u2}}{\tan \beta_2} \tag{14}$$

where the total temperature at the impeller exit T_{t2} equals to the measured one T_{t6} at the volute exit when neglecting heat transfer effects. Thermodynamic state variables can be computed as follows:

$$T_2 = T_{t2} - \frac{c_{u2}^2 + c_{m2}^2}{2c_p} \tag{15}$$

$$\rho_2 = \frac{p_2}{RT_2} \tag{16}$$

where the static pressure p_2 is the mean pressure measured by transducer II-2, II-4, II-5, and II-6. Consider the continuity equation:

$$\rho_1 A_1 B_1 c_{m1} = \rho_2 A_2 B_2 c_{m2} \tag{17}$$

where the meridional velocity at the impeller inlet can be computed from the measured inlet volumetric flow, and the ratio of blockage factors $B_{1\text{-}2} = B_2/B_1$ is assumed. Finally, the flow angle can be resolved by solving the above equations.

Given different ratios of blockage factors, the increment in the flow angle is presented in Fig. 21. For cases with the same ratio of blockage factors after installing the casing treatment device, the maximum flow angle increment is about 1.2 degrees, which may be too small to make an impact. Those changes are mainly due to the slip factor, indicating its relatively low contribution to the increased flow angle. For cases with a larger ratio of blockage factors after applying the casing treatment device, the increment in the flow angle is more substantial than their counterparts. The effect of reducing the impeller exit blockage has been checked in preliminary CFD results, where the blockage factor is calculated as follows:

$$B = \frac{\int c_m dA}{\int dA} \cdot \frac{\int \rho c_m dA}{\int \rho c_m^2 dA} \tag{18}$$

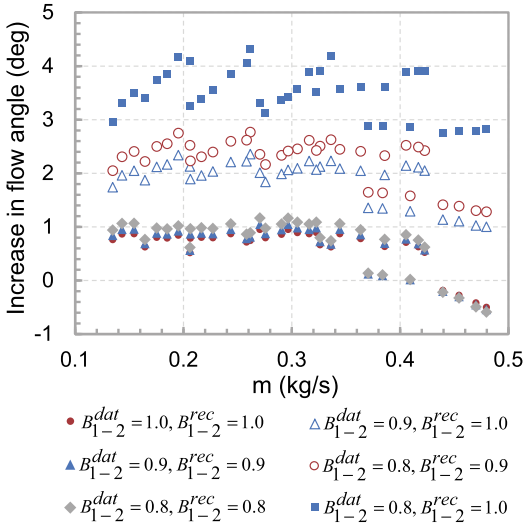

Fig. 21. The increment of the absolute flow angle by the casing treatment.

At 0.34 kg/s and 90% speed near the onset of the mild surge, the blockage factor is found to increase from 0.73 to 0.91, and the flow angle has risen by 4.4 degrees. Thus, the casing treatment device increases the impeller exit flow angle mainly by reducing the impeller exit blockage. In a recent study, the blockage factor at the impeller exit is modeled by the flow coefficient, the impeller tip Mach number, and the impeller inlet-to-exit area ratio [35]. Modifications concerning the casing treatment device are needed in the future.

6. Discussions

In this research, the casing treatment device is capable of eliminating rotating instability and stall at low speeds, as well as delaying the onset of deep surge at high speeds. However, mild surge still exists at middle and high speeds, which constrains the application of the compressor. Experimental evidence suggests that the casing treatment increases the incidence at the vaned diffuser inlet, and thus deteriorates the vaned diffuser stability. In other words, the matching between the impeller and the vaned diffuser of the test compressor has been changed by the casing treatment device. Such changes are supposed to be general for cases with an evident blockage at the datum impeller exit and a large recirculation flow rate inside the casing treatment device.

A straightforward way to eliminate mild surge is to re-match the impeller and the vaned diffuser by reducing the diffuser throat (e.g., design a pinch part at the vaneless space, reduce the radial gap ratio, increase the vane setting angle, etc.). The drawback of those modifications is a reduced choke mass flow, which still limits the potential of the casing treatment device.

To further develop its potential, flow control methods are recommended in the vaned diffuser. Several previous studies have highlighted the significance of the tornado-shaped vortex at the vaned diffuser inlet in determining the instability onset [13–15]. In previous numerical studies of the current case, a large incidence near the casing was captured at the vaned diffuser inlet [36], which could trigger vortex sheddings, and thus initiate the flow instability. Flow control methods including flow suction [13], flow injection and obstruction [37,38], and inducement of a vane tip clearance [39,40] at the vaned diffuser inlet are some of the successful examples in extending the stable flow range. Combination of flow control techniques at both the impeller inlet and the vaned diffuser inlet is worth researching in the future.

7. Conclusions

The paper investigates the roles of self-recirculation casing treatment on compressor flow instabilities across scales. Rig tests and transient pressure measurements are conducted on a high pressure ratio centrifugal compressor with and without a casing treatment device. Several conclusions are drawn as follows:

1. Casing treatment devices are effective in constraining flow instabilities across temporal and spatial scales. Its potential in improving the stability of a high pressure ratio centrifugal compressor with a vaned diffuser has been demonstrated at an extensive range of operating speeds.
2. Casing treatment devices can eliminate the impeller inlet rotating instability and stall that usually occur at low speeds. The detected rotating instability and stall are featured as backward traveling vortical flows. The casing treatment device establishes a flow recirculation process, which relieves the impeller inlet blockage, removes the vortical structures, and thus eliminates rotating instability and stall.
3. Casing treatment devices can suppress the surge phenomenon of the compression system at middle and high speeds, although surge is initiated by the downstream vaned diffuser. The casing treatment device improves the compressor stage stability by turning the impeller pressure rise characteristics more negative, which is achieved by enhancing the impeller work input. The magnitude of the work input increment is determined by the recirculation ratio and the work input ratio. However, the casing treatment reduces the impeller exit blockage, increases the incidence at the vaned diffuser inlet, and thus leads to a more positive slope of the vaned diffuser pressure rise characteristics. The potential of the casing treatment could be further developed by applying flow control techniques at the vaned diffuser.

Conflict of interest statement

None declared.

Acknowledgement

This research was supported by the National Natural Science Foundation of China (Grant No. 51876097). The authors would like to thank Wuxi Itma Turbo Technologies for the assistance of experiments. Special thanks to colleagues from Tsinghua Turbomachinery Laboratory: Mr. David Pannen conducted preliminary numerical simulations, Ms. Wenchao Zhang and Mr. Aolin Wang helped prepare the experiment, and Mr. Zitian Niu and Mr. Wangzhi Zou helped analyze the data.

References

[1] H. Krain, Review of centrifugal compressor's application and development, J. Turbomach. 127 (1) (2005) 25–34.
[2] D. Japikse, Centrifugal Compressor Design and Performance, Concepts ETI Inc., Wilder, VT, 1996.
[3] I.J. Day, Stall, surge, and 75 years of research, J. Turbomach. 138 (1) (2016) 011001.
[4] N. Cumpsty, Compressor Aerodynamics, Kreiger Publishing Company, Malabar, FL, 2004.
[5] E.M. Greitzer, Surge and rotating stall in axial flow compressors, part I: theoretical compression system model, J. Eng. Power 98 (2) (1976) 190–198.
[6] H. Emmons, C. Pearson, H. Grant, Compressor Surge and Stall Propagation, American Society of Mechanical Engineers Paper 53-A-65, 1955.
[7] R. Mailach, I. Lehmann, K. Vogeler, Rotating instabilities in an axial compressor originating from the fluctuating blade tip vortex, J. Turbomach. 123 (3) (2001) 453–460.
[8] J. Marz, C. Hah, W. Neise, An experimental and numerical investigation into the mechanisms of rotating instability, J. Turbomach. 124 (3) (2002) 367–374.
[9] X. Zheng, A. Liu, Experimental investigation of surge and stall in a high-speed centrifugal compressor, J. Propuls. Power 31 (3) (2015) 815–825.
[10] X. Zheng, Z. Sun, T. Kawakubo, H. Tamaki, Experimental investigation of surge and stall in a turbocharger centrifugal compressor with a vaned diffuser, Exp. Therm. Fluid Sci. 82 (2017) 493–506.
[11] V. Moënne-Loccoz, I. Trébinjac, E. Benichou, S. Goguey, B. Paoletti, P. Laucher, An experimental description of the flow in a centrifugal compressor from alternate stall to surge, J. Therm. Sci. 26 (4) (2017) 289–296.
[12] X. He, X. Zheng, Flow instability evolution in high pressure ratio centrifugal compressor with vaned diffuser, Exp. Therm. Fluid Sci. 98 (2018) 719–730.
[13] Z.S. Spakovszky, C.H. Roduner, Spike and modal stall inception in an advanced turbocharger centrifugal compressor, J. Turbomach. 131 (3) (2009) 031012.
[14] Y. Bousquet, N. Binder, G. Dufour, X. Carbonneau, M. Roumeas, I. Trebinjac, Numerical simulation of stall inception mechanisms in a centrifugal compressor with vaned diffuser, J. Turbomach. 138 (12) (2016) 121005.
[15] N. Fujisawa, Y. Ohta, Transition process from diffuser stall to stage stall in a centrifugal compressor with a vaned diffuser, Int. J. Rotating Mach. 2017 (2017) 2861257.
[16] H. Chen, V.M. Lei, Casing treatment and inlet swirl of centrifugal compressors, J. Turbomach. 135 (4) (2013) 041010.
[17] H. Khaleghi, Effect of discrete endwall recirculation on the stability of a high-speed compressor rotor, Aerosp. Sci. Technol. 37 (2014) 130–137.
[18] E. Guillou, M. Gancedo, E. Gutmark, A. Mohamed, PIV investigation of the flow induced by a passive surge control method in a radial compressor, Exp. Fluids 53 (3) (2012) 619–635.
[19] B. Semlitsch, M. Mihaescu, Flow phenomena leading to surge in a centrifugal compressor, Energy 103 (2016) 572–587.
[20] G.A. Christou, Fluid Mechanics of Ported Shroud Centrifugal Compressor for Vehicular Turbocharger Applications, Ph.D. Thesis, MIT, Cambridge, MA, 2015.
[21] D. Pannen, Investigation of Flow Control Methods to Extend the Stable Range of an 8.0 Pressure Ratio Centrifugal Compressor, Master Thesis, Tsinghua University, China, 2016.
[22] H. Tamaki, Effect of recirculation device with counter swirl vane on performance of high pressure ratio centrifugal compressor, J. Turbomach. 134 (5) (2012) 051036.
[23] R. Numakura, H. Tamaki, H. Hazby, M. Casey, Effect of a Recirculation Device on the Performance of Transonic Mixed Flow Compressors, American Society of Mechanical Engineers Paper GT2014-25365, 2014.
[24] Y. Ma, G. Xi, G. Wu, An Impact of Self-Recirculation Casing Treatment (SRCT) Configurations on Impeller Stall Margin and the Flow Field, American Society of Mechanical Engineers Paper GT2012-68335, 2012.
[25] S. Sivagnanasundaram, S. Spence, J. Early, B. Nikpour, An impact of various shroud bleed slot configurations and cavity vanes on compressor map width and the inducer flow field, J. Turbomach. 135 (4) (2013) 041003.
[26] S. Sivagnanasundaram, S. Spence, J. Early, Map width enhancement technique for a turbocharger compressor, J. Turbomach. 136 (6) (2014) 061002.
[27] C. Park, Y. Choi, K. Lee, J. Yoon, Numerical study on the range enhancement of a centrifugal compressor with a ring groove system, J. Mech. Sci. Technol. 25 (2) (2012) 1371–1378.
[28] M. Yang, R. Martinez-Botas, Y. Zhang, X. Zheng, Effect of self-recirculation-casing treatment on high pressure ratio centrifugal compressor, J. Propuls. Power 32 (1) (2016) 602–610.
[29] X. Zheng, Y. Zhang, M. Yang, T. Bamba, H. Tamaki, Stability improvement of high-pressure-ratio turbocharger centrifugal compressor by asymmetrical flow control, part II: nonaxisymmetrical self-recirculation casing treatment, J. Turbomach. 135 (2) (2013) 021007.
[30] J. Xiao, W. Xu, C. Gu, X. Shu, Self-recirculating casing treatment for a radial compressor, Chin. J. Mech. Eng. 22 (4) (2009) 567–573.
[31] M. Inoue, M. Kuroumaru, T. Tanino, S. Yoshida, M. Furukawa, Comparative studies on short and long length-scale stall cell propagating in an axial compressor rotor, J. Turbomach. 123 (1) (2001) 24–30.
[32] E. Guillou, M. Gancedo, E. Gutmark, Experimental investigation of flow instability in a turbocharger ported shroud compressor, J. Turbomach. 138 (6) (2016) 061002.
[33] S. Yamaguchi, H. Yamaguchi, S. Goto, H. Nakao, F. Nakamura, The development of effective casing treatment for turbocharger compressors, in: IMechE Seventh International Conference on Turbochargers and Turbocharging, London, May 17–18, 2002, pp. 23–32.
[34] J.N. Everitt, Z.S. Spakovszky, D. Rusch, J. Schiffmann, The role of impeller outflow conditions on the performance of vaned diffusers, J. Turbomach. 139 (4) (2017) 041004.
[35] C. Stuart, S. Spence, D. Filsinger, A. Starke, S. Kim, Characterizing the influence of impeller exit recirculation on centrifugal compressor work input, J. Turbomach. 140 (1) (2018) 011005.
[36] X. He, X. Zheng, J. Wei, H. Zeng, Investigation of Vaned Diffuser Splitters on the Performance and Flow Control of High Pressure Ratio Centrifugal Compressors, American Society of Mechanical Engineers Paper GT2016-56255, 2016.
[37] G.J. Skoch, Experimental investigation of centrifugal compressor stabilization techniques, J. Turbomach. 125 (4) (2003) 704–713.

[38] G.J. Skoch, Experimental investigation of diffuser Hub injection to improve centrifugal compressor stability, J. Turbomach. 127 (1) (2005) 107–117.
[39] S. Ubben, R. Niehuis, Experimental investigation of the diffuser vane clearance effect in a centrifugal compressor stage with adjustable diffuser geometry, part I: compressor performance analysis, J. Turbomach. 137 (3) (2015) 031003.
[40] S. Ubben, R. Niehuis, Experimental investigation of the diffuser vane clearance effect in a centrifugal compressor stage with adjustable diffuser geometry, part II: detailed flow analysis, J. Turbomach. 137 (3) (2015) 031004.